Article

Fully Transparent and Sensitivity-Programmable Amorphous Indium-Gallium-Zinc-Oxide Thin-Film Transistor-Based Biosensor Platforms with Resistive Switching Memories

Hyeong-Un Jeon and Won-Ju Cho *

Department of Electronic Materials Engineering, Kwangwoon University, 20 Gwangun-ro, Nowon-gu, Seoul 01897, Korea; wjsguddns9154@kw.ac.kr
* Correspondence: chowj@kw.ac.kr; Tel.: +82-2-940-5163; Fax: +82-2-943-5163

Abstract: This paper presents a fully transparent and sensitivity-programmable biosensor based on an amorphous-indium-gallium-zinc-oxide (*a*-IGZO) thin-film transistor (TFT) with embedded resistive switching memories (ReRAMs). The sensor comprises a control gate (CG) and a sensing gate (SG), each with a resistive switching (RS) memory connected, and a floating gate (FG) that modulates the channel conductance of the *a*-IGZO TFT. The resistive coupling between the RS memories connected to the CG and SG produces sensitivity properties that considerably exceed the limit of conventional ion-sensitive field-effect transistor (ISFET)-based sensors. The resistances of the embedded RS memories were determined by applying a voltage to the CG–FG and SG–FG structures independently and adjusting the compliance current. Sensors constructed using RS memories with different resistance ratios yielded a pH sensitivity of 50.5 mV/pH (R_{CG}:R_{SG} = 1:1), 105.2 mV/pH (R_{CG}:R_{SG} = 2:1), and 161.9 mV/pH (R_{CG}:R_{SG} = 3:1). Moreover, when the R_{CG}:R_{SG} = 3:1, the hysteresis voltage width (V_H) and drift rate were 54.4 mV and 32.9 mV/h, respectively. As the increases in V_H and drift rate are lower than the amplified sensitivity, the sensor performs capably. The proposed device is viable as a versatile sensing device capable of detecting various substances, such as cells, antigens, DNA, and gases.

Keywords: amorphous oxide semiconductor; ion-sensitive field-effect transistor; resistive coupling effect; embedded resistive switching memories; multi-level state

Citation: Jeon, H.-U.; Cho, W.-J. Fully Transparent and Sensitivity-Programmable Amorphous Indium-Gallium-Zinc-Oxide Thin-Film Transistor-Based Biosensor Platforms with Resistive Switching Memories. *Sensors* **2021**, *21*, 4435. https://doi.org/10.3390/s21134435

Academic Editors: Marco Mugnaini and Ada Fort

Received: 20 May 2021
Accepted: 25 June 2021
Published: 28 June 2021

Publisher's Note: MDPI stays neutral with regard to jurisdictional claims in published maps and institutional affiliations.

Copyright: © 2021 by the authors. Licensee MDPI, Basel, Switzerland. This article is an open access article distributed under the terms and conditions of the Creative Commons Attribution (CC BY) license (https://creativecommons.org/licenses/by/4.0/).

1. Introduction

In response to the increasing interest in personal health and the demand for smart healthcare technology, extensive research is being conducted on sensors that can detect hygiene conditions, diseases, biological signals, and water quality directly [1,2]. In particular, field-effect transistor (FET)-based sensors offer advantageous properties such as low feature size, high integration density, short response time, and accurate sensing operation [2–5]. However, typical ion-sensitive FETs (ISFETs) based on bulk silicon substrates are confined by the Nernst limit (a theoretical sensitivity limit of 59.14 mV/pH), which impedes their real-life application and commercialization [6–8]. As an alternative, silicon-on-insulator (SOI)-based dual-gate ISFETs are attracting attention owing to their ability to overcome the Nernst limit via the capacitive coupling effect between the upper and lower gate oxides of the channel layer. Nevertheless, the commercial development of dual-gate ISFETs on SOI substrates faces several challenges, such as complexity involving the fabrication of multiple capacitors, expensive substrate materials, and limitations regarding the physical properties of silicon. Recently, our group proposed a sensitivity amplification technique based on the resistive coupling effect to counteract this restriction [9]. Compared to the capacitive coupling effect, resistive coupling is freed from the intrinsic restrictions of the SOI substrate material by constructing coplanar resistors, which are cost effective and reduce the processing time. In our previous report, we used coplanar-type resistors with

fixed resistances, meaning that sensitivity amplification was determined via pattern design. As the sensitivity of ISFETs depends mainly on the ion concentration of the detection target and the chemical sensitivity of its surface, flexible sensitivity amplification is desirable to increase application diversity [10–15]. In this study, we propose a fully transparent and sensitivity-programmable biosensor based on an amorphous indium-gallium-zinc-oxide (*a*-IGZO) thin-film transistor (TFT) and embedded resistive switching memory (ReRAM). To ensure the cost effectiveness and full transparency of the transducers, the *a*-IGZO TFTs were fabricated on glass substrates. The fundamental TFT structure comprises a triple gate consisting of a control gate (CG), sensing gate (SG), and floating gate (FG) to provide high sensitivity through resistive coupling. In addition, as a variable resistor for sensitivity adjustment, we applied ReRAM comprising metal–insulator–metal (ITO/Ta_2O_5/ITO) structures that provide non-volatile multi-level cell (MLC) properties. The resistive switching (RS) memory is embedded between the CG and FG (CG–FG) and between the SG and FG (SG–FG), and the CG and SG resistances (R_{CG}, R_{SG}) can be adjusted independently using set and reset operations. Furthermore, we introduced a separate extended gate (EG) sensing unit to prevent damage caused by the direct exposure of the metal gate of the transducer to pH buffer solutions. This configuration improved the reliability and stability of the transducer, thereby enabling the easy replacement of damaged sensing membranes and guaranteeing their cost effectiveness. To evaluate the performance of the transducer components, we measured the RS characteristics and resistance distribution of the ITO/Ta_2O_5/ITO RS memory and the electrical characteristics of the *a*-IGZO TFT. After programming the resistances of the built-in RS memories, the pH sensitivity was measured according to the resistive coupling ratio of R_{CG} and R_{SG}, resulting in a high sensitivity beyond the Nernst limit. In addition, to verify the long-term stability and reliability, non-ideal behaviors such as hysteresis and drift effects were evaluated.

2. Materials and Methods

2.1. Fabrication of Transducer and Sensing Units for Sensitivity-Programmable Biosensor

Fully transparent *a*-IGZO TFTs with embedded RS memories based on a metal–insulator–metal (ITO/Ta_2O_5/ITO) structure were fabricated on 1 × 1 cm glass substrates (Corning Inc., New York, USA). After performing the standard RCA chemical cleaning process, a bottom FG electrode consisting of a 150-nm-thick ITO conductive film was deposited on a glass substrate using an RF magnetron sputtering system and defined using photolithography and lift-off processes. Subsequently, 60-nm-thick Ta_2O_5 and 60-nm-thick SiO_2 films were deposited sequentially using RF magnetron sputtering to produce the FG insulator. For the channel layer, a 50-nm-thick *a*-IGZO film was deposited using a sputter target comprising In_2O_3, Ga_2O_3, and ZnO in a ratio of 4:2:4.1 mol%. Elemental analysis of the *a*-IGZO TFT channel was performed by X-ray photoelectron spectroscopy (XPS), in which uniform concentrations of In, Ga, Zn, and O were distributed in the depth direction, and the ratio of In:Ga:Zn was 4:2:4.1. The *a*-IGZO active channel region, which had a width of 20 μm and a length of 10 μm, was defined via photolithography and wet etching processes. Then, an ITO film with a thickness of 150 nm was deposited before the source/drain (S/D) electrode was formed using the lift-off method. Local etching of the 60 nm thick SiO_2 film, which stacked on the 60 nm thick Ta_2O_5 film, was conducted via a combination of photolithography and wet etching with a buffered oxide etchant (BOE, in a ratio of 30:1) to form contact holes for the CG and SG on the FG, with the Ta_2O_5 film acting as an RS memory switching layer. After depositing a 150 nm thick ITO conductive film, the CG and SG were formed on the Ta_2O_5 RS layer via a lift-off process, thereby completing the top electrode (TE) of the embedded RS memory. Additionally, the local contact area of the bottom electrode (BE) of the RS memory was defined using photolithography to create contact holes on the SiO_2/Ta_2O_5 stacked layer on the FG electrode, before being etched via reactive ion etching (RIE).

Finally, microwave annealing was performed at a power of 1000 W for 2 min in ambient O_2 to improve the electrical properties of the *a*-IGZO TFT and the embedded RS

memory. We performed X-ray diffraction (XRD) analysis on the as-deposited and MWA-annealed *a*-IGZO films to confirm that both were in the amorphous state. The top-view and conceptual cross-sectional structures of the *a*-IGZO TFT-based transducer with embedded ReRAMs are illustrated in Figure 1a,b, respectively.

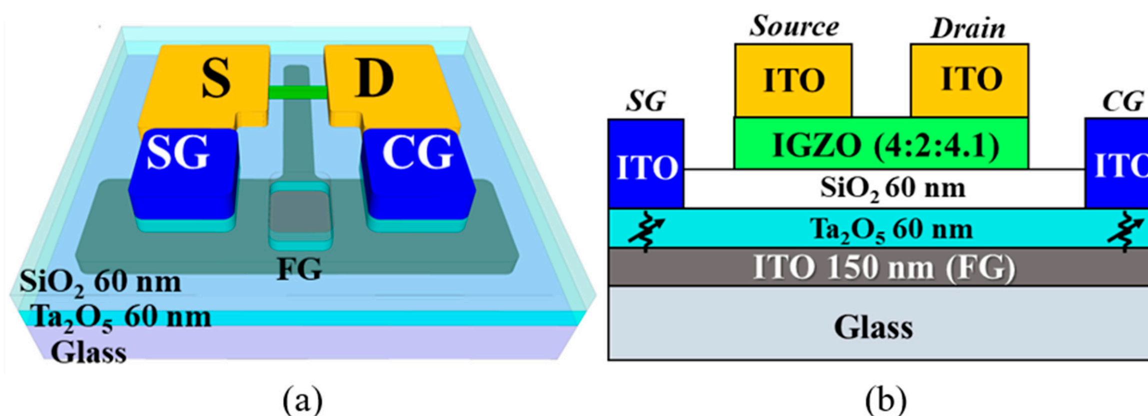

Figure 1. Schematic diagrams illustrating the (**a**) top-view and (**b**) conceptual cross-sectional structures of the *a*-IGZO TFT transducer with embedded ReRAMs on a glass substrate.

The EG for pH buffer solution detection was prepared by depositing a 300 nm thick ITO conductive film followed by a 50 nm thick SnO_2 sensing membrane on a 1.5 × 2.5 cm glass substrate, and then attaching a poly-dimethyl siloxane (PDMS) reservoir to store the pH buffer solution. All the film thicknesses were measured through the DektakXT stylus profilometer (Bruker, Billerica, MA, USA) (not shown thickness data in here). Figure 2a,b show a microscope image and a photograph of the fabricated *a*-IGZO TFT transducer and the EG, respectively. Figure 2c shows the optical transmittance of the fabricated *a*-IGZO TFT transducer, which was measured over a wavelength range of 380–700 nm using an Agilent 8453 UV-visible spectrophotometer.

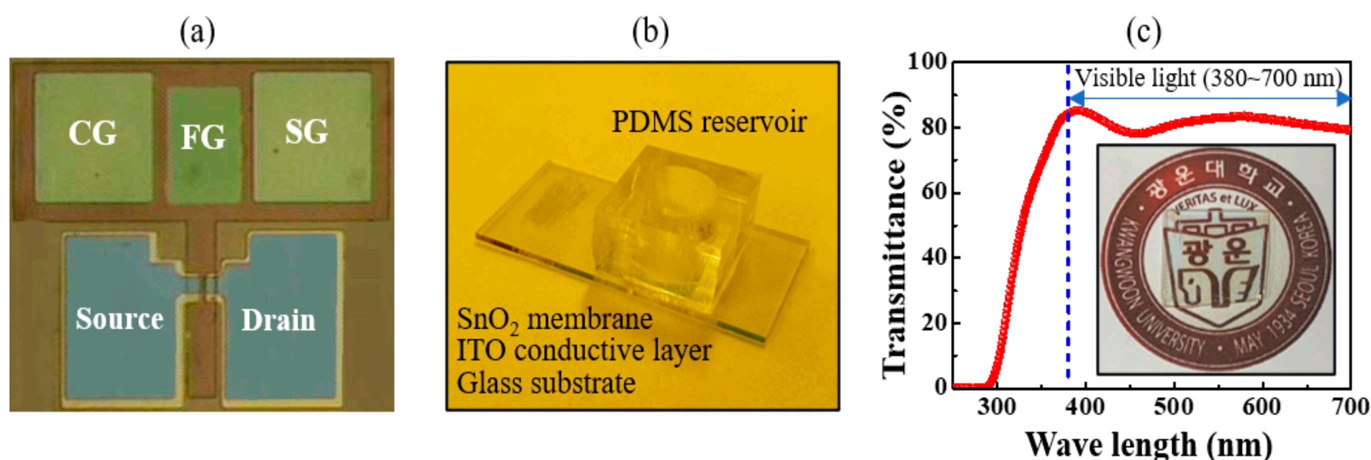

Figure 2. (**a**) Microscope image of the fabricated *a*-IGZO TFT transducer and (**b**) photograph of the fabricated EG. These parts were fabricated independently on separate glass substrates. (**c**) Optical transmittance and photograph (inset) of the fully transparent *a*-IGZO TFT transducer.

2.2. Characterization of Sensitivity-Programmable Biosensor

The electrical properties of the constructed sensors were measured using an Agilent 4156B Precision Semiconductor Parameter Analyzer and probe station system in a dark box to exclude illuminance and electrical interference. A commercial Ag/AgCl electrode (Horiba 2080A-06T) consisting of a ceramic–plug junction and an internal solution saturated with KCl and AgCl was utilized as a reference electrode for pH detection. The potential of the pH buffer solution was measured by connecting the *a*-IGZO TFT transducer and EG directly with an electric wire—the configuration of the electrical measurement system is shown in Figure 3. The sensitivity was determined by measuring the changes in the CG voltage (defined as the reference voltage, V_R) at a drain current of 1 nA (defined as the reference current, I_R) as a function of the pH value. In addition, the hysteresis and drift voltages were measured to identify the non-ideal behavior of the proposed sensor. The hysteresis voltage width was defined as the difference between the V_R of the first and last pH values in the following pH loop sequence: $7 \rightarrow 10 \rightarrow 7 \rightarrow 4 \rightarrow 7$. To evaluate the drift phenomenon, the V_R was monitored while exposing the EG to a pH 7 buffer solution for 10 h, with the drift rate defined as the change in V_R (ΔV_R).

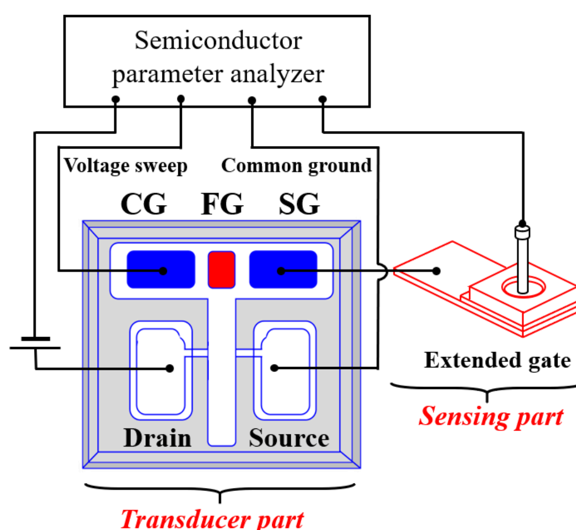

Figure 3. Configuration of the measurement system. The FG serves as the common BE of the embedded RS memories, while the CG and SG serve as the TE.

3. Results and Discussion

3.1. Resistive Coupling Effect Simulations

Figure 4 shows the simulation results (performed in PSpice) of the potential for signal amplification using resistive coupling effects, which predicts the electrical properties that may occur during practical measurements in the absence of physical and electrical interference. In addition, by excluding conduction due to unexpected tunneling phenomena, such as Fowler–Nordheim tunneling, the tunneling of conduction band electrons, trap assisted tunneling, direct quantum tunneling, and Schottky tunneling, it is possible to observe the shift of the transfer characteristics (via drain current versus gate voltage curves at a fixed drain voltage) according to the resistance ratio change with accuracy. Figure 4a shows a simplified equivalent circuit for simulating the resistive coupling effect, where V_{CG} and V_{SG} represent the voltages applied to the CG and SG, respectively, and R_{CG} and R_{SG} represent the external resistors connected in series to the CG and SG. The voltage across the FG is resistively coupled to the R_{CG} and R_{SG}, as expressed by Equation (1) (in terms of voltage distribution), while the voltage across the CG is described by Equation (2). Consequently,

Equation (3) can be derived, which describes the amplification of the potential modulation across the CG (ΔV_{CG}) owing to the potential across the SG (ΔV_{SG}) at a ratio of R_{CG}/R_{SG}:

$$V_{FG} = \left(\frac{R_{SG}}{R_{CG} + R_{SG}}\right)V_{CG} + \left(\frac{R_{CG}}{R_{CG} + R_{SG}}\right)V_{SG} \tag{1}$$

$$V_{CG} = \left(\frac{R_{CG} + R_{SG}}{R_{SG}}\right)V_{FG} - \left(\frac{R_{CG}}{R_{SG}}\right)V_{SG} \tag{2}$$

$$\Delta V_{CG} \propto \left(\frac{R_{CG}}{R_{SG}}\right)\Delta V_{SG}. \tag{3}$$

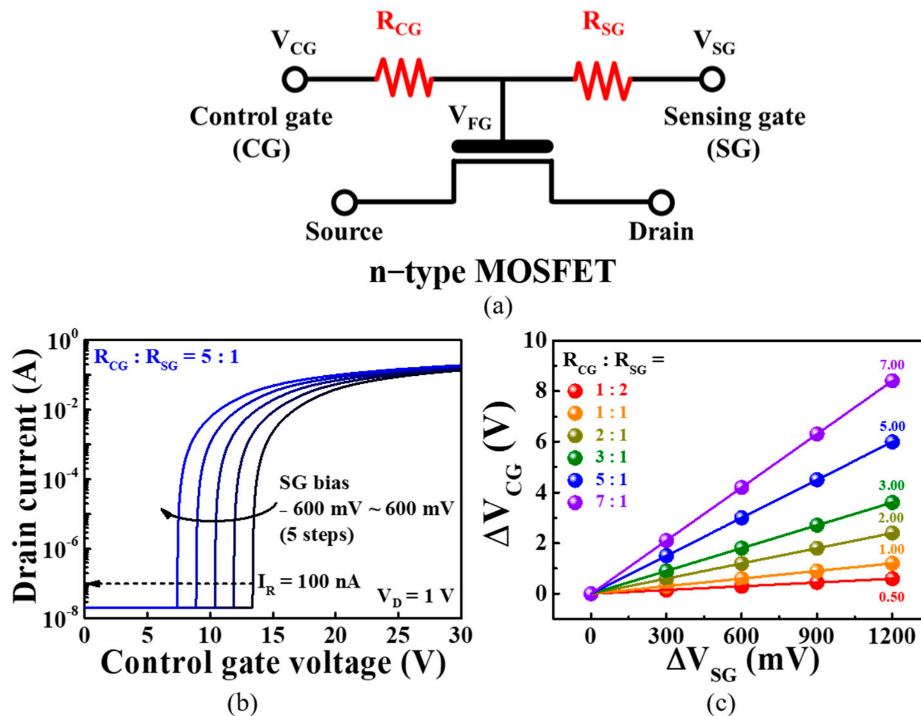

Figure 4. (**a**) Simplified equivalent circuit corresponding to the PSpice simulation of the sensitivity amplification due to the resistive coupling effect; (**b**) transfer characteristic curve shift as a function of V_{SG}; (**c**) plot of $\Delta V_{CG}/\Delta V_{SG}$ according to the amplification factor R_{CG}/R_{SG}.

Figure 4b shows the PSpice simulation of conventional n-type MOSFET transfer characteristic ($I_D - V_G$) curves when the R_{CG}:R_{SG} = 5:1 and V_D = 0.05 V, as a typical case. As the V_{SG} increases from −600 to 600 mV in 300 mV intervals, the transfer curve shifts in the negative direction. Figure 4c plots the magnitude of ΔV_{CG} as a function of V_{SG} for R_{CG}:R_{SG} = 1:2, 1:1, 2:1, 3:1, 5:1, and 7:1. It is observed that the shift in the transfer characteristic curve increases according to the amplification factor (R_{CG}/R_{SG}) as R_{CG} increases.

3.2. RS Characteristics of ITO/Ta_2O_5/ITO-Structured RS Memory

Through the resistance change and non-volatile memory characteristics of the embedded RS memory of the ITO/Ta_2O_5/ITO structure, it is possible to decipher a continuous arbitrary resistance ratio for the fabricated sensor platform. Figure 5a exhibits the forming/rupturing process for a conducting filament (CF) in conventional metal-oxide-based RS memory. Owing to the insulating properties of the metal-oxide layer, the initial RS layer prohibits current from flowing between the TE and the BE, thus necessitating a forming process that introduces arbitrary defects into the resistance change characteristics. The forming process induces the soft breakdown of the initial RS layer by applying a strong

electric field to the TE, creating oxygen vacancies (i.e., lattices in which oxygen ions are separated) and contributing to the formation of a CF through which electrons move [16–20]. At this point, an appropriate compliance current (I_C) must be set to prevent the hard breakdown of the RS layer. Then, oxygen ions in the RS layer move according to the polarity of the electric field applied to the TE and combine with the oxygen vacancies to form and rupture CFs, with the TE acting as an "oxygen reservoir" that accumulates or releases oxygen ions. Based on this mechanism, the resistance state of the RS layer, which can be determined by the field polarity and the magnitude of the voltage applied to the TE, can be adjusted [18,20]. Figure 5b shows the typical bipolar resistive switching (BRS) *I–V* characteristics of the ITO/Ta_2O_5/ITO stack used in the constructed sensors, where the red and blue lines represent the high-resistance and low-resistance states (HRS and LRS), respectively. We measured the BRS characteristics at 0.01 V intervals while adjusting the voltage applied to the TE according to the following sequence: 0 V → 2 V → −1.2 V → 0 V, while setting the I_C to 1.4 mA to prevent the hard breakdown of the RS layer [16–18,20]. As the positive voltage applied to the TE increases, the Ta_2O_5 RS layer remains in an HRS until an abrupt increase in the current occurs above 0.8 V, as indicated by the "set" process labeled (1) in Figure 5b. During the "set" process, oxygen vacancies in the RS layer form CFs and the Ta_2O_5 RS layer becomes an LRS, resulting in a decrease in resistance, as illustrated in Figure 5a. This LRS holds irrespective of whether the voltage decreases, and the polarity is reversed; however, it changes again at a voltage of −1.2 V, whereupon the "reset" process, labeled (2) in Figure 5b, takes effect. At this point, oxygen ions stored in the TE are released into the RS layer via repulsive forces and combine with oxygen vacancies to form CFs. As a result, the CF in the RS layer ruptures and the resistance in the Ta_2O_5 RS layer increases, with the resistance in the RS layer "reset" to a HRS. This suggests that the fabricated ITO/Ta_2O_5/ITO structure can be used as an embedded variable resistor that realizes programmable sensitivity by combining resistance switching with nonvolatile memory characteristics. Inset of Figure 5b are resistance endurance of HRS and LRS at a read voltage (V_{read}) of 0.2 V. The average R_{HRS}/R_{LRS} was ~7.3, indicating that the embedded ReRAM has stable BRS endurance over 1×10^2 DC cycles. Figure 5c shows the cumulative resistance distributions for LRS and HRS over 1×10^2 sequential DC cycles. It is found that the embedded ReRAM with ITO/Ta_2O_5/ITO structure has a stable resistance distribution. The average resistances (R_{HRS}, R_{LRS}) and standard deviations (σ_{HRS}, σ_{LRS}) of the HRS and LRS were $R_{HRS} = 8 \times 10^3\ \Omega$ ($\sigma_{HRS} = 0.48 \times 10^3\ \Omega$) and $R_{LRS} = 1.1 \times 10^3\ \Omega$ ($\sigma_{LRS} = 0.07 \times 10^3\ \Omega$), respectively.

Figure 6 shows the experimental results for the multi-level characteristics of the ITO/Ta_2O_5/ITO-structured RS memory. The size of the CF can be modified by adjusting the I_C, which is often used to control the resistance of the RS layer. As the size of CF increases, the amount of current flowing between the TE and BE increases, thereby enabling multiple LRS levels at the same voltage [17,21,22]. Figure 6a shows the *I–V* curves as the I_C is varied from 0.9 to 1.4 mA in the "set" region where a positive voltage is applied to the TE, which is enlarged around the V_{read} to distinguish the resistance differences between LRS levels. Depending on the I_C, a single HRS and five LRSs were identified, with the resistances of these states extracted using $V = IR$ at the V_{read} of 0.2 V. To conduct a quantitative comparison and verify the uniformity of the resistance in response to repeated switching, we evaluated the RS operation 30 times for each resistance state as shown in Figure 6b. Figure 6c shows the retention characteristics for non-volatile multiple level resistance over 10^4 s. The six resistance states do not change for 10^4 s, providing a stable non-volatile retention characteristic. Table 1 summarizes the average resistance (μ) and standard deviation (σ) of the multi-level resistance states. As the I_C increases, the LRS resistances and their standard deviations decrease, indicating that a sensitivity-programmable sensor can be implemented using the resistive coupling of multi-level R_{CG} and R_{SG} resistors.

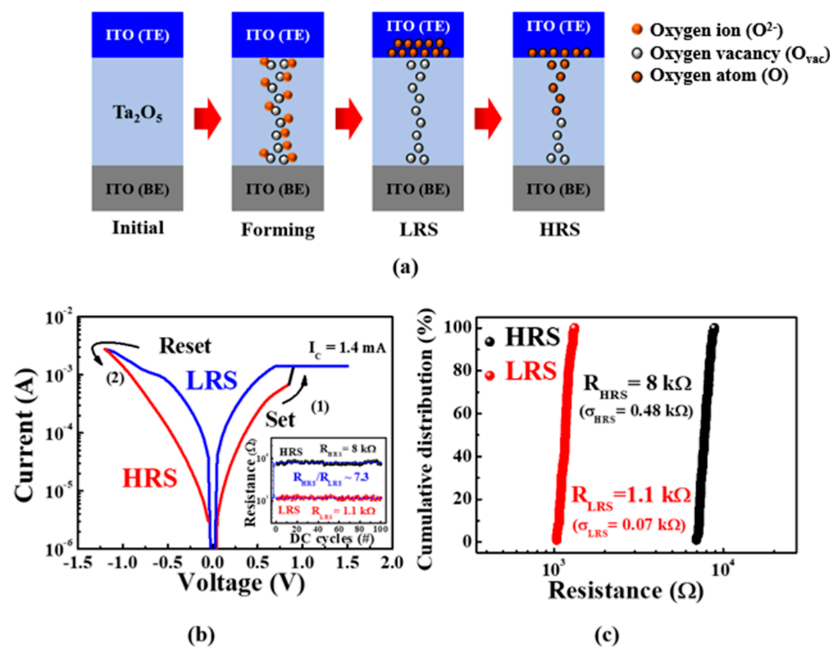

Figure 5. (**a**) Schematic of formation and rupturing of conductive filaments (CFs) in the Ta_2O_5 RS layer; (**b**) BRS *I*-V characteristics curves of ITO/Ta_2O_5/ITO RS layer. Inset shows resistance endurance of HRS and LRS at a read voltage (V_{read}) of 0.2 V; (**c**) cumulative resistance distribution during 1×10^2 sequential DC cycles.

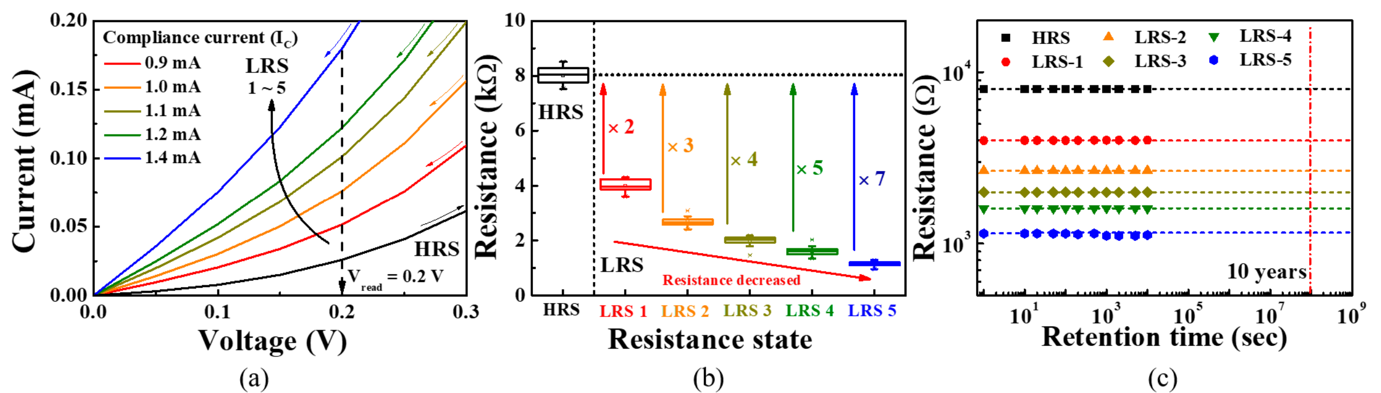

Figure 6. Evaluation of multi-level resistance states in ITO/Ta_2O_5/ITO-structured RS memory for different I_C values. (**a**) Multi-level BRS *I–V* curves at V_{read} = 0.2 V; (**b**) resistance distribution and (**c**) non-volatile retention performance during 10^4 s of the multi-level resistance states.

Table 1. Average resistance and standard deviation (σ) of the resistance states in ITO/Ta_2O_5/ITO-structured RS memory.

Resistance State	*R* (kΩ)	σ (kΩ)
HRS	7.99	0.30
LRS-1 (I_C = 0.9 mA)	3.99	0.19
LRS-2 (I_C = 1.0 mA)	2.63	0.14
LRS-3 (I_C = 1.1 mA)	2.05	0.13
LRS-4 (I_C = 1.2 mA)	1.62	0.13
LRS-5 (I_C = 1.4 mA)	1.14	0.08

3.3. Electrical Characteristics of a-IGZO TFT-Based Transducer Units

Figure 7 shows the electrical characteristics of the *a*-IGZO TFT owing to the operation of the bottom FG. The performance of the transducer greatly influences the sensing operation of the entire pH sensor platform. The proposed fully transparent *a*-IGZO TFTs fabricated on glass substrates exhibit excellent electrical properties. For the transfer characteristic ($I_D - V_G$) curves in Figure 7a, the threshold voltage (V_{th}), on/off current ratio (I_{on}/I_{off}), field-effect mobility (μ_{FE}), and subthreshold swing (SS) were −0.44 V, 7.58 × 10^5, 14.67 cm^2/V·s, and 127.2 mV/dec, respectively. In addition, the interfacial trap density (D_{it}) between the gate insulator and the *a*-IGZO channel degrades the mobility and stability of the transducer, causing non-ideal behavior during sensing. It was calculated using the following equation [23,24]:

$$D_{it} = \left(\frac{SSlog(e)}{kT/q} - 1\right)\frac{C_i}{q}, \quad (4)$$

where q, k, T, and C_i represent the unit charge, Boltzmann constant, absolute temperature, and capacitance per unit area, respectively. For the proposed *a*-IGZO TFT-based transducer, we determined D_{it} to be 3.48 × 10^{11} cm^{-2}. For the output characteristic ($I_D - V_D$) curves in Figure 7b, the ohmic contact between the *a*-IGZO channel and the ITO source/drain was identified by the linear increase in I_D with V_D in the small V_D region, while a pinch-off phenomenon, whereby the I_D gradually saturates in the large V_D region, is also observed.

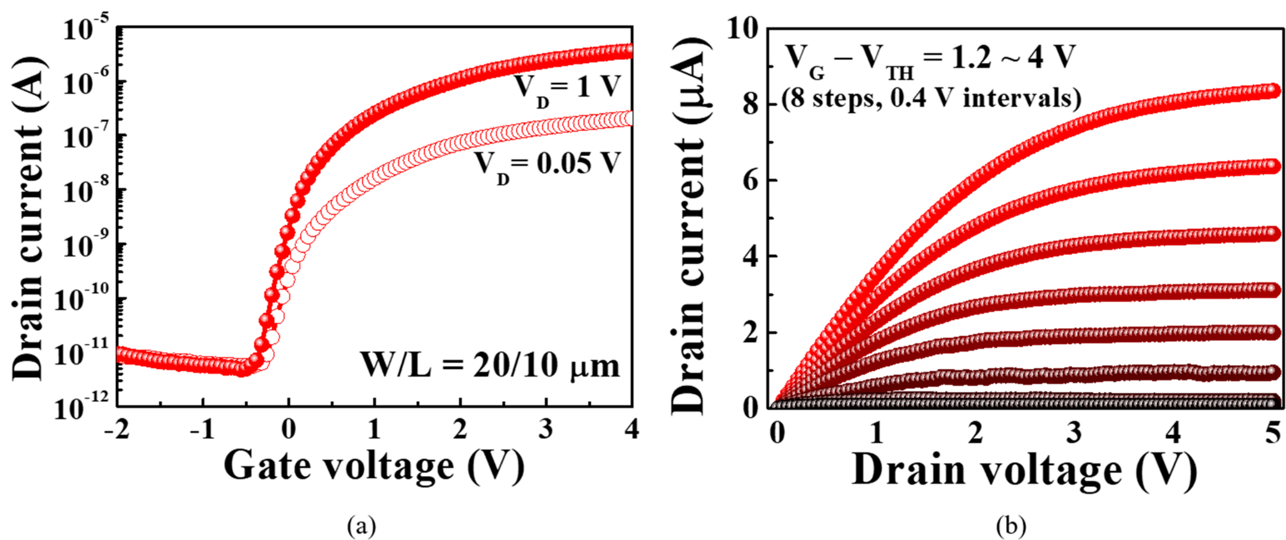

Figure 7. (**a**) Transfer characteristic and (**b**) output characteristic curves of the *a*-IGZO TFT-based transducer in response to the operation of the bottom FG.

3.4. pH-Sensing Characteristics of Sensitivity-Programmable Biosensor Platform

In general, the pH sensitivity at room temperature cannot exceed 59.14 mV/pH because of the Nernst limitation [6]. According to the site-binding theory, the pH-dependency of the surface potential (ψ) is given by

$$\psi = 2.303\frac{kT}{q}\frac{\beta}{\beta+1}(pH_{pzc} - pH), \quad (5)$$

where pH_{pzc} is the pH value with zero free charges and β is the constant representing the chemical sensitivity of the sensing surface [7]. Thus, the value of ψ depends on the number of ions in the pH solution and the chemical sensitivity of the sensing surface. The sensitivity amplification of the proposed sensor is implemented through the following mechanisms. First, the change in the surface potential ($\Delta\psi$) of the membrane in the EG unit owing to the change in the pH value of the buffer solution is transferred to the SG electrode

of the transducer unit, thereby changing the V_{SG}. Then, the V_{CG} (voltage across the CG electrode) connected in series with the SG electrode via the FG electrode is changed by $V_{SG} \cdot (R_{CG}/R_{SG})$ owing to the resistive coupling, as described by Equation (2). As a result, the transfer characteristic curve corresponding to the V_{CG} sweep shifts by R_{CG}/R_{SG}, while the reference voltage (V_R) is changed by the same magnitude. Finally, the sensitivity of the proposed sensor is amplified by R_{CG}/R_{SG}. Figure 8a–c show the pH sensing characteristics of the sensitivity-programmable sensors. The resistance states of the R_{SG} were programmed as HRS, LRS-1, and LRS-2, which are chosen as typical resistance states in this study, while the R_{CG} remained as HRS.

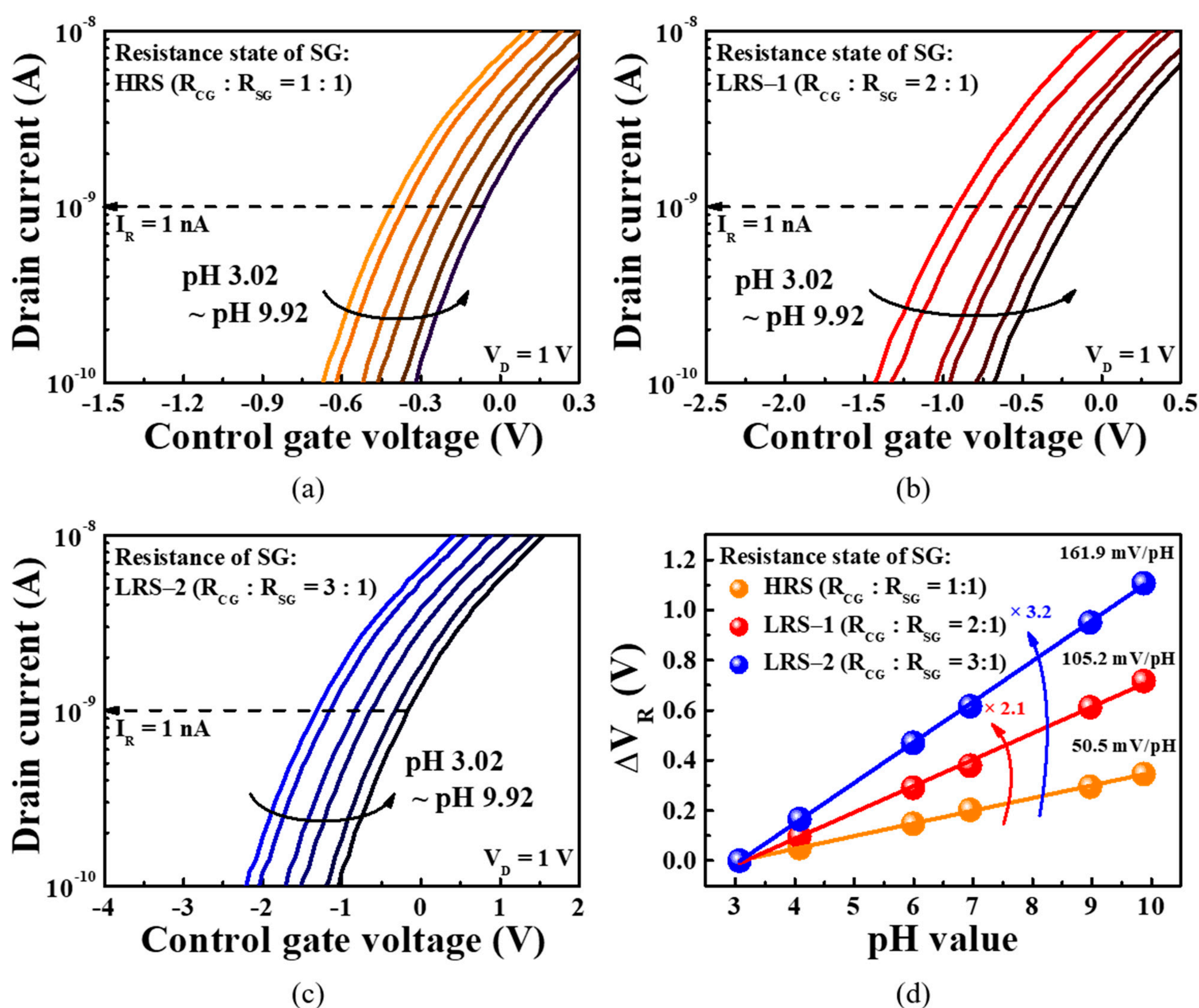

Figure 8. Transfer curves of the *a*-IGZO TFT transducer with ITO/Ta_2O_5/ITO-structured RS memory for SG resistance states of (**a**) HRS (R_{CG}:R_{SG} = 1:1); (**b**) LRS-1 (R_{CG}:R_{SG} = 2:1); (**c**) LRS-2 (R_{CG}:R_{SG} = 3:1) in various pH buffer solutions; (**d**) pH sensitivity for various R_{CG}:R_{SG} resistance ratios.

The resistance according to each resistance state is mentioned in Table 2, and when R_{SG} is programmed as HRS, LRS-1, and LRS-2, the resistance ratio R_{CG}:R_{SG} is 1:1, 2:1, and 3:1, respectively. Sensitivity measurements were performed using buffer solutions with pH concentrations of 3.02, 4.07, 5.98, 6.99, 8.98, and 9.92, and the transfer curve was obtained by sweeping the CG voltage. The magnitude of the transfer curve shift was determined using the reference drain current (I_R, 1 nA), and thus the magnitude of transfer curve shift is represented by the reference voltage shift (ΔV_R). Figure 8d shows

the ΔV_R as a function of the pH value. For R_{SG} = HRS (R_{CG}:R_{SG} = 1:1), the pH sensitivity was 50.5 mV/pH, which is lower than the Nernst limit of 59.14 mV/pH. However, for R_{SG} = LRS-1 and LRS-2 (R_{CG}:R_{SG} = 2:1 and 3:1), the pH sensitivities were 105.2 and 161.9 mV/pH, respectively, exceeding the Nernst limit comfortably. Furthermore, the sensitivities according to R_{CG}/R_{SG} exhibit a linearity of 99.9%. These results demonstrate that the proposed sensitivity-programmable sensor provides flexible pH detection in various situations owing to the tunability of the amplification factor.

Table 2. Summary of the pH sensing characteristics of the fabricated sensitivity-programmable sensor.

Resistance State of R_{SG}	Sensitivity (mV/pH)		V_H (mV)		Drift Rate (mV/h)	
	Measured	Amplified	Measured	Amplified	Measured	Amplified
HRS	50.5	1	34.5	1	29.0	1
LRS-1 (R_{CG}:R_{SG} = 2:1)	105.2	2.08	45.4	1.31	30.4	1.04
LRS-2 (R_{CG}:R_{SG} = 3:1)	161.9	3.21	57.4	1.66	32.9	1.13

As the sensing membrane is exposed directly to the pH buffer for a long time, surface defects caused by diverse ions give rise to non-ideal effects, which degrades the accuracy and reliability of the device [25–30]. We measured the hysteresis and drift effects to evaluate the reliability and stability of the sensitivity-programmable sensor. Hysteresis is the change in electrical properties due to the gradual reaction between the surface of the sensing membrane and the ions in the buffer solution, while the drift indicates the change in the electrical properties due to ionic penetration from the surface into the sensing membrane [25,26].

Figure 9a shows the hysteresis effect measured by immersing the membrane in pH buffer solutions. The magnitude of the hysteresis voltage was measured as the V_R difference between the initial and final pH states of the pH loop in which the buffer solution was changed at 10 min intervals according to the following sequence: pH 7 → pH 10 → pH 7 → pH 4 → pH 7. The hysteresis voltage widths were 34.5, 45.4, and 57.4 mV for R_{SG} states of HRS (R_{CG}:R_{SG} = 1:1), LRS-1 (R_{CG}:R_{SG} = 2:1), and LRS-2 (R_{CG}:R_{SG} = 3:1), respectively. Figure 9b shows the evolution of the drift effect over a 10 h period in a pH 7 buffer solution. Drift rates of 29.0, 30.4, and 32.9 mV/h were recorded for R_{SG} states of HRS, LRS-1, and LRS-2, respectively. Table 2 summarizes the pH sensing characteristics of the fabricated sensitivity-programmable sensor. Compared to the R_{SG} states of HRS (R_{CG}:R_{SG} = 1:1), the R_{SG} states of LRS-1 (R_{CG}:R_{SG} = 2:1) has 2.08 times higher sensitivity, 1.33 times greater V_H, and 1.04 times higher drift rate, while when the R_{SG} states of LRS-2 (R_{CG}:R_{SG} = 3:1) has 3.21 times higher sensitivity, 1.66 times larger V_H, and 1.13 times higher drift rate. Note that although the pH sensitivity of the proposed device shows a linear increase regarding the R_{CG}:R_{SG} resistance ratio, non-ideal behaviors such as the V_H and the drift rate are not affected significantly by these resistance ratios, thus highlighting the potential of the fabricated device as a high-performance sensor platform.

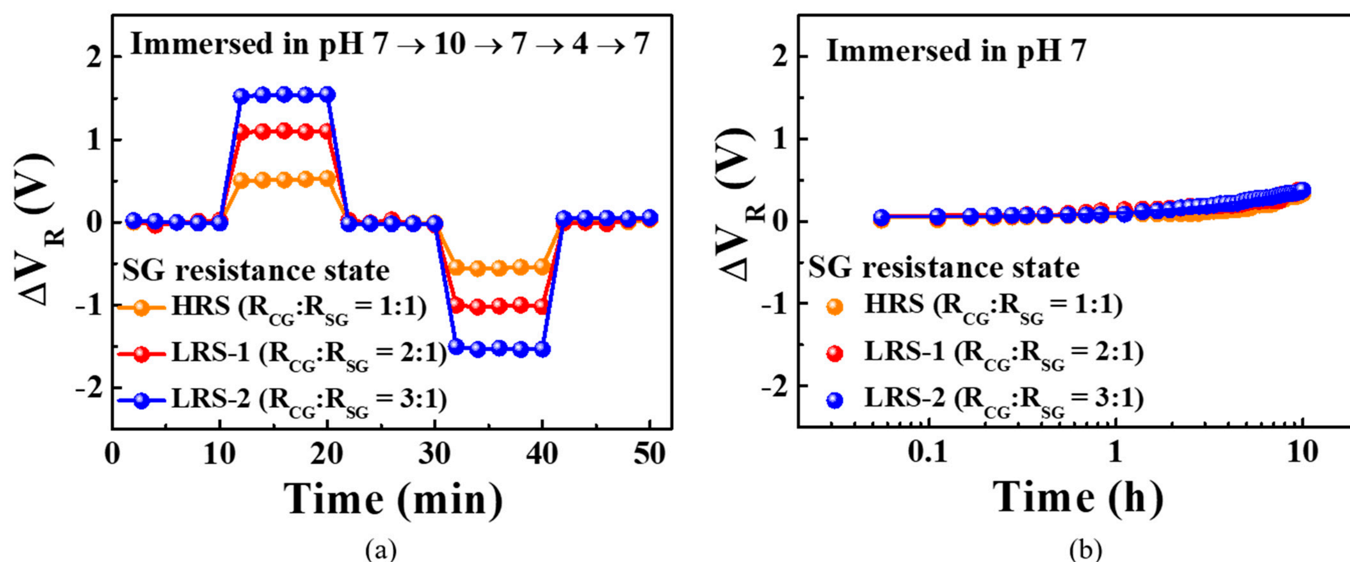

Figure 9. (**a**) Hysteresis and (**b**) drift effects for the sensitivity-programmable *a*-IGZO ISTFT sensor with embedded ITO/Ta_2O_5/ITO RS memory. Non-ideal effects were monitored for SG resistance states of HRS (R_{CG}:R_{SG} = 1:1), LRS-1 (R_{CG}:R_{SG} = 2:1), and LRS-2 (R_{CG}:R_{SG} = 3:1).

4. Conclusions

In this paper, we propose a fully transparent and sensitivity-programmable biosensor platform based on an *a*-IGZO TFT with embedded ITO/Ta_2O_5/ITO RS memory. Using PSpice simulations, we calculated the sensitivity amplification caused by the resistive coupling of the R_{CG} in the CG electrode and the R_{SG} in the SG electrode, which were connected in series via the FG electrode. The *a*-IGZO TFT, which has a significant influence on the sensing operation, is fully transparent and fabricated on a glass substrate and exhibits excellent electrical characteristics as a transducer for the proposed sensor platform. In addition, the embedded RS memories of metal–insulator–metal (ITO/Ta_2O_5/ITO) structure between CG–FG and between SG–FG exhibits bipolar switching behavior, providing non-volatile multi-level cell (MLC) characteristics. The various resistances of the embedded RS memories were implemented by independently applying voltage to CG–FG and SG–FG and adjusting I_C. Through this, the sensitivity of the *a*-IGZO TFT transducer with embedded ITO/Ta_2O_5/ITO RS memory provides various pH sensitivity according to the resistance states programmed in the RS memories embedded in the CG and SG electrodes. For programmed resistance ratios of R_{CG}:R_{SG} = 1:1, 2:1, and 3:1, the pH sensitivity exhibited 50.5, 105.2, and 161.9 mV/pH, respectively, thereby demonstrating the feasibility of exceeding the Nernst limit (59.14 mV/pH). In addition, to verify non-ideal effects, we evaluated the hysteresis and drift effects, revealing that the increases in the hysteresis voltage width and drift rate are lower than the sensitivity amplification, confirming the suitability of the proposed sensor platform for high-performance sensor applications. In conclusion, the proposed platform displays immense promise for applications involving the detection of diverse substances containing different amounts of ions such as cells, antigens, antibodies, DNA, and gases or for self-calibrating differences in chemical sensitivity.

Author Contributions: H.-U.J.: conceptualization, formal analysis, methodology, investigation, data curation, visualization, software, resources, and writing—original draft. W.-J.C.: conceptualization, methodology, investigation, resources, formal analysis, funding acquisition, supervision, validation, and writing—review and editing. All authors have read and agreed to the published version of the manuscript.

Funding: This research was supported by the National Research Foundation of Korea (NRF) grant funded by the Korea government (MIST) (No. 2020R1A2C1007586). The work was also funded and conducted under [The competency development program for industry specialists] of the Ko-

rean Ministry of Trade, Industry and Energy (MOTIE), operated by Korea Institute for Advancement of Technology (KIAT) (No. P0002397, HRD program for Industrial Convergence of Wearable Smart Devices).

Data Availability Statement: The data presented in this study are available from the corresponding author upon reasonable request.

Acknowledgments: The research has been conducted by the Research Grant of Kwangwoon University in 2021 and by the excellent research support project of Kwangwoon University in 2021. This work was also supported by the National Research Foundation of Korea (NRF) grant funded by the Korea government (MSIT) (No. 2020R1A2C1007586). The work was also funded and conducted under [The competency development program for industry specialists] of the Korean Ministry of Trade, Industry and Energy (MOTIE), operated by Korea Institute for Advancement of Technology (KIAT) (No. P0002397, HRD program for Industrial Convergence of Wearable Smart Devices).

Conflicts of Interest: The authors declare no conflict of interest.

References

1. St John, A.; Price, C.P. Existing and emerging technologies for point-of-care testing. *Clin. Biochem. Rev.* **2014**, *35*, 155–167.
2. Lee, C.-S.; Kim, S.K.; Kim, M. Ion-sensitive field-effect transistor for biological sensing. *Sensors* **2009**, *9*, 7111–7131. [CrossRef] [PubMed]
3. Moser, N.; Lande, T.S.; Toumazou, C.; Georgiou, P. ISFETs in CMOS and emergent trends in instrumentation: A review. *IEEE Sensors J.* **2016**, *16*, 6496–6514. [CrossRef]
4. Vu, C.-A.; Chen, W.-Y. Field-effect transistor biosensors for biomedical applications: Recent advances and future prospects. *Sensors* **2019**, *19*, 4214. [CrossRef]
5. Park, J.-K.; Cho, W.-J. Development of high-performance fully depleted silicon-on-insulator based extended-gate field-effect transistor using the parasitic bipolar junction transistor effect. *Appl. Phys. Lett.* **2012**, *101*, 133703. [CrossRef]
6. Bergveld, P. Development of an ion-sensitive solid-state device for neurophysiological measurements. *IEEE Trans. Biomed. Eng.* **1970**, *17*, 70–71. [CrossRef]
7. Yates, D.E.; Levine, S.; Healy, T.W. Site-binding model of the electrical double layer at the oxide/water interface. *J. Chem. Soc. Faraday Trans.* **1974**, *70*, 1807–1818. [CrossRef]
8. Jang, H.-J.; Gu, J.-G.; Cho, W.J. Sensitivity enhancement of amorphous InGaZnO thin film transistor based extended gate field-effect transistors with dual-gate operation. *Sens. Actuators B Chem.* **2013**, *181*, 880–884. [CrossRef]
9. Cho, S.-K.; Cho, W.-J. High-Sensitivity pH Sensor Based on Coplanar Gate AlGaN/GaN Metal-Oxide-Semiconductor High Electron Mobility Transistor. *Chemosensors* **2021**, *9*, 42. [CrossRef]
10. Pullano, S.A.; Critello, C.D.; Mahbub, I.; Tasneem, N.T.; Shamsir, S.; Islam, S.K.; Greco, M.; Fiorillo, A.S. EGFET-based sensors for bioanalytical applications: A review. *Sensors* **2018**, *18*, 4042. [CrossRef]
11. Chi, L.-L.; Choub, J.-C.; Chung, W.-Y.; Sunc, T.-P.; Hsiung, S.K. Study on extended gate field effect transistor with tin oxide sensing membrane. *Mater. Chem. Phys.* **2000**, *63*, 19–23. [CrossRef]
12. Yang, C.-M.; Wang, I.-S.; Lin, Y.-T.; Huang, C.-H.; Lu, T.-F.; Lue, C.-E.; Pijanowska, D.G.; Hua, M.-Y.; Lai, C.-S. Low cost and flexible electrodes with NH_3 plasma treatments in extended gate field effect transistors for urea detection. *Sens. Actuators B Chem.* **2013**, *187*, 274–279. [CrossRef]
13. Das, A.; Ko, D.H.; Chen, C.-H.; Chang, L.-B.; Lai, C.-S.; Chu, F.-C.; Chow, L.; Lin, R.-M. Highly sensitive palladium oxide thin film extended gate FETs as pH sensor. *Sens. Actuators B Chem.* **2014**, *205*, 199–205. [CrossRef]
14. Chien, Y.-S.; Tsai, W.-L.; Lee, I.-C.; Chou, J.-C.; Cheng, H.-C. A novel pH sensor of extended-gate field-effect transistors with laser-irradiated carbon-nanotube network. *IEEE Electron Device Lett.* **2012**, *33*, 1622–1624. [CrossRef]
15. Chen, J.-C.; Chou, J.-C.; Sun, T.-P.; Hsiung, S.-K. Portable urea biosensor based on the extended-gate field effect transistor. *Sens. Actuators B Chem.* **2003**, *91*, 180–186. [CrossRef]
16. Prakash, A.; Hwang, H. Multilevel cell storage and resistance variability in resistive random access memory. *Phys. Sci. Rev.* **2016**, *1*, 50–57.
17. Wong, H.-S.P.; Lee, H.-Y.; Yu, S.; Chen, Y.-S.; Wu, Y.; Chen, P.-S.; Lee, B.; Chen, F.T.; Tsai, M.-J. Metal–oxide RRAM. *IEEE Proc.* **2012**, *100*, 1951–1970. [CrossRef]
18. Ielmini, D. Resistive switching memories based on metal oxides: Mechanisms, reliability and scaling. *Semicond. Sci. Technol.* **2016**, *31*, 063002. [CrossRef]
19. Yen, T.J.; Gismatulin, A.; Volodin, V.; Gritsenko, V.; Chin, A. All nonmetal resistive random access memory. *Sci. Rep.* **2019**, *9*, 6144. [CrossRef]
20. Kumar, D.; Chand, R.A.U.; Tseng, T.Y. Metal oxide resistive switching memory: Materials, properties and switching mechanisms. *Ceram. Int.* **2017**, *43*, S547–S556. [CrossRef]
21. Prakash, A.; Park, J.; Song, J.; Woo, J.; Cha, E.; Hwang, H. Demonstration of low power 3-bit multilevel cell characteristics in a TaO_x-based RRAM by stack engineering. *IEEE Electron Device Lett.* **2014**, *36*, 32–34. [CrossRef]

22. Russo, U.; Kamalanathan, D.; Ielmini, D.; Lacaita, A.L.; Kozicki, M.N. Study of multilevel programming in programmable metallization cell (PMC) memory. *IEEE Trans. Electron Devices* **2009**, *56*, 1040–1047. [CrossRef]
23. Sze, S.M.; Li, Y.; Ng, K.K. *Physics of Semiconductor Devices*, 4th ed.; John Wiley & Sons: Hoboken, NJ, USA, 2021; p. 944.
24. Li, J.; Huang, C.-X.; Zhang, J.-H.; Zhu, W.-Q.; Jiang, X.-Y.; Zhang, Z.-L. Temperature stress on a thin film transistor with a novel BaZnSnO semiconductor using a solution process. *RSC Adv.* **2015**, *5*, 9621–9626. [CrossRef]
25. Bousse, L.; Bergveld, P. The role of buried OH sites in the response mechanism of inorganic-gate pH-sensitive ISFETs. *Sens. Actuators* **1984**, *6*, 65–78. [CrossRef]
26. Shahriar, J.; Collins, S.; Smith, R.L. A physical model for drift in pH ISFETs. *Sens. Actuators B Chem.* **1998**, *49*, 146–155.
27. Garde, A.; Alderman, J.; Lane, W. Improving the Drift and Hysteresis of the Si_3N_4 pH Response Using RTP Techniques. *Sens. Mater.* **1997**, *9*, 15–24.
28. Chou, J.C.; Hsiao, C.N. The hysteresis and drift effect of hydrogenated amorphous silicon for ISFET. *Sens. Actuators B Chem.* **2000**, *66*, 181–183. [CrossRef]
29. Bousse, L.; Van Den Vlekkert, H.H.; De Rooij, N.F. Hysteresis in Al_2O_3-gate ISFETs. *Sens. Actuators B Chem.* **1990**, *2*, 103–110. [CrossRef]
30. Hein, P.; Egger, P. Drift behaviour of ISFETs with Si_3N_4-SiO_2 gate insulator. *Sens. Actuators B Chem.* **1993**, *14*, 655–656. [CrossRef]